Supporting Information for Strong Coupling in Bulk Nanoplasmonic Nanoplatelet Perovskite Scintillators

Michal Makowski[1*], Dominik Kowal[1], Anna Pniakowska[1], Kamil Misztal[1,2], Mohanad S. Eid[3], Joanna Cybinska[1,4], Winicjusz Drozdowski[3], Benoit Mahler[6], Christophe Dujardin[5,6], Detlef Hommel[1,7], Liang Jie Wong[9,10], Dennis R. Schaart[11,12], Sergio Brovelli[13,14], Muhammad Danang Birowosuto[1*]

[1]Lukasiewicz Research Network - PORT Polish Center for Technology Development, Wroclaw, 54-066, Poland.
[2]Department of Semiconductor Materials Engineering, Wrocław University of Science and Technology, Wroclaw, 50-370, Poland.
[3]Institute of Physics, Faculty of Physics, Astronomy, and Informatics, Nicolaus Copernicus University in Torun, Torun, 87-100, Poland.
[4]Faculty of Chemistry, University of Wroclaw, Wroclaw, 50-383, Poland.
[5]Universite Claude Bernard Lyon 1, Institut Lumiere Matiere UMR 5306 CNRS, 10 rue Ada Byron, Villeurbanne, 69622, France.
[6]Institut Universitaire de France (IUF), 1 rue Descartes, Paris Cedex 05, 75231, France.
[7]Institute of Low Temperature and Structure Research, Polish Academy of Sciences, 50-422 Wroclaw, Poland.
[9]CINTRA (CNRS-International-NTU-THALES Research Alliance), IRL 3288 Research Techno Plaza, 50 Nanyang Drive, Border X Block, Level 6, Singapore 637553, Singapore.
[10]School of Electrical and Electronic Engineering, Nanyang Technological University, Singapore 639798, Singapore.
[11]Delft University of Technology, Radiation Science & Technology dept., 2629JB, Delft, The Netherlands.
[12]HollandPTC, 2629JH, Delft, The Netherlands.
[13]Department of Physics, University of Milano-Bicocca, 20126 Milan, Italy.
[14]INFN–Sezione di Milano-Bicocca, 20126, Milan, Italy.

*Corresponding author(s). E-mail(s):
michal.makowski@port.lukasiewicz.gov.pl;
muhammad.birowosuto@port.lukasiewicz.gov.pl;

List of Figures

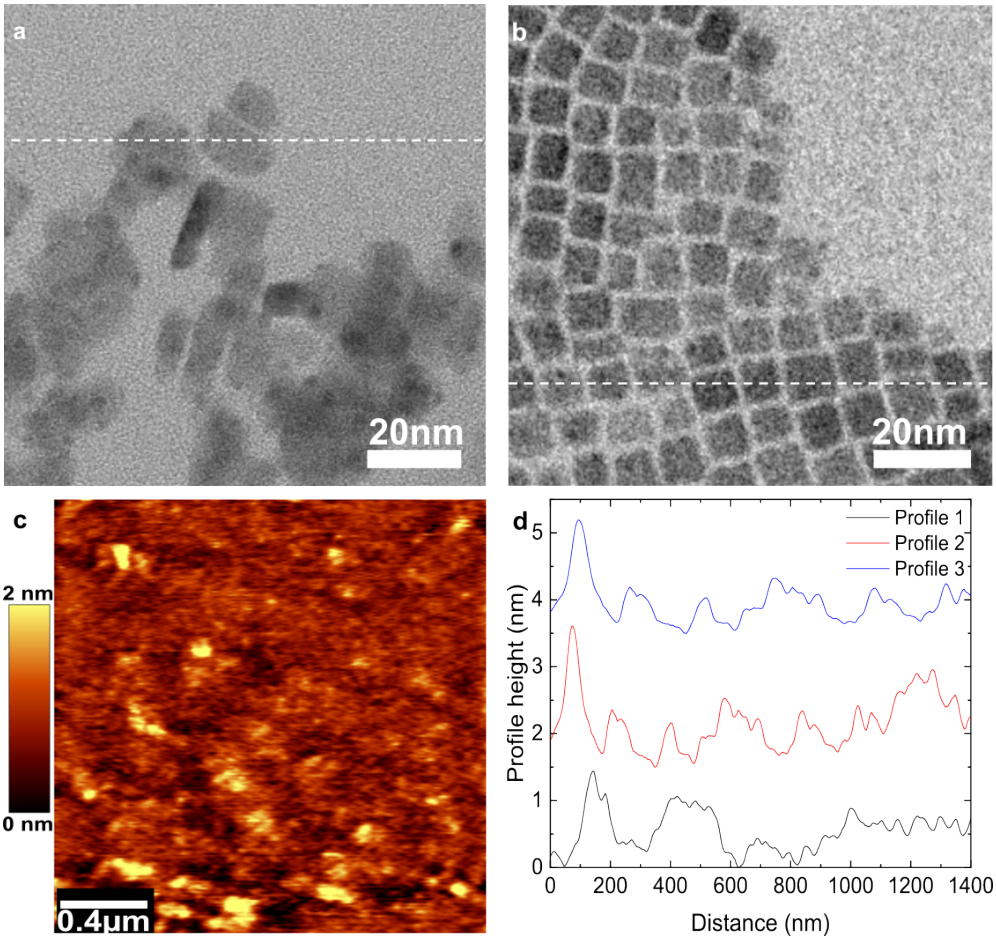

Fig. S1 Transmission electron microscopy (TEM) and atomic force microscopy (AFM) characterization. (**a**) TEM image of $CsPbBr_3$ nanoplatelets (NPLs). (**b**) TEM image of $CsPbBr_3$ nanocrystals (NCs). (**c**) AFM topography map. (**d**) Corresponding surface line profiles.

Morphology

Transmission electron microscopy (TEM) imaging was performed using an FEI Tecnai G2 T20 X-Twin microscope (FEI Company) operated at an accelerating voltage of 200 kV. The samples were deposited onto carbon-coated copper grids and left to dry in ambient conditions before being placed in the microscope chamber. Imaging was carried out at various magnifications depending on the particle size. WITec Atomic Force Microscope was employed for AFM characterisation.

From both types of analysis the thickness of $CsPbBr_3$ NPLs is evaluated to be 1.93 $\pm$ 0.38 nm.

Optical properties

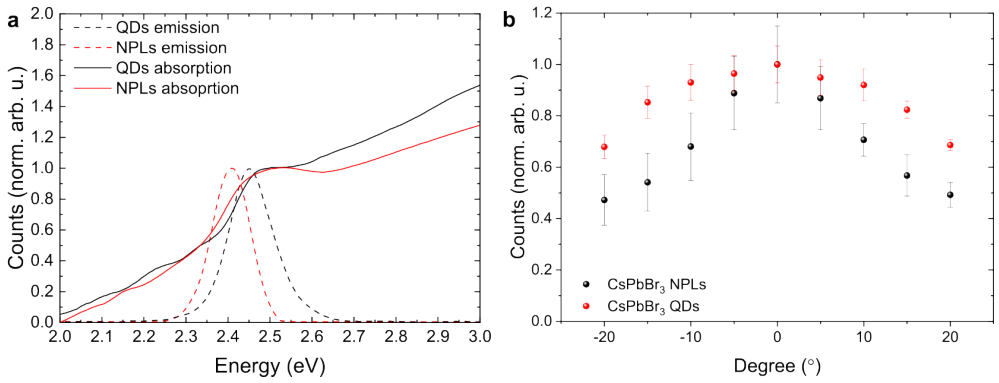

Fig. S2 Optical properties of $CsPbBr_3$ nanostructures. a, Absorption (solid) and photoluminescence (PL) (dashed) spectra of $CsPbBr_3$ NPLs (red) and NCs (black). **b**, Angle-resolved PL spectra collected over emission angles from $-20°$ to $20°$.

Absorption spectra were measured with a commercially available Filmetrics F10-RTA-UV analyser. Angle-resolved PL spectra were collected under 405 nm laser excitation, and the signal was collected with the NA 0.06 objective.

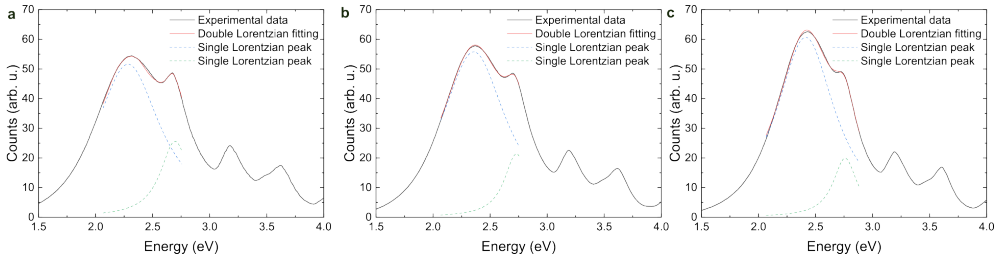

Fig. S3 Room-temperature scattering spectra of $CsPbBr_3$/Ag composites. Measured spectra with double-Lorentzian fits for composites containing cubic nanoparticles (CNPs) of side length (**a**) 85 nm, (**b**) 80 nm, and (**c**) 75 nm.

The experimental spectra were fitted using the sum of Lorentzian components defined as

$$I(E) = \sum_{i=1}^{2} A_i \frac{\left(\frac{1}{2}\Gamma_i\right)^2}{(E - E_i)^2 + \left(\frac{1}{2}\Gamma_i\right)^2}, \tag{S1}$$

where E is the photon energy (in meV), E_i denote the resonance energies of the individual peaks, Γ_i are their full widths at half maximum (FWHM), and A_i are amplitudes proportional to the peak intensities. All parameters (E_i, Γ_i, A_i) were treated as free

variables and optimised by nonlinear least-squares fitting using the `curve_fit` routine from the SciPy library[1].

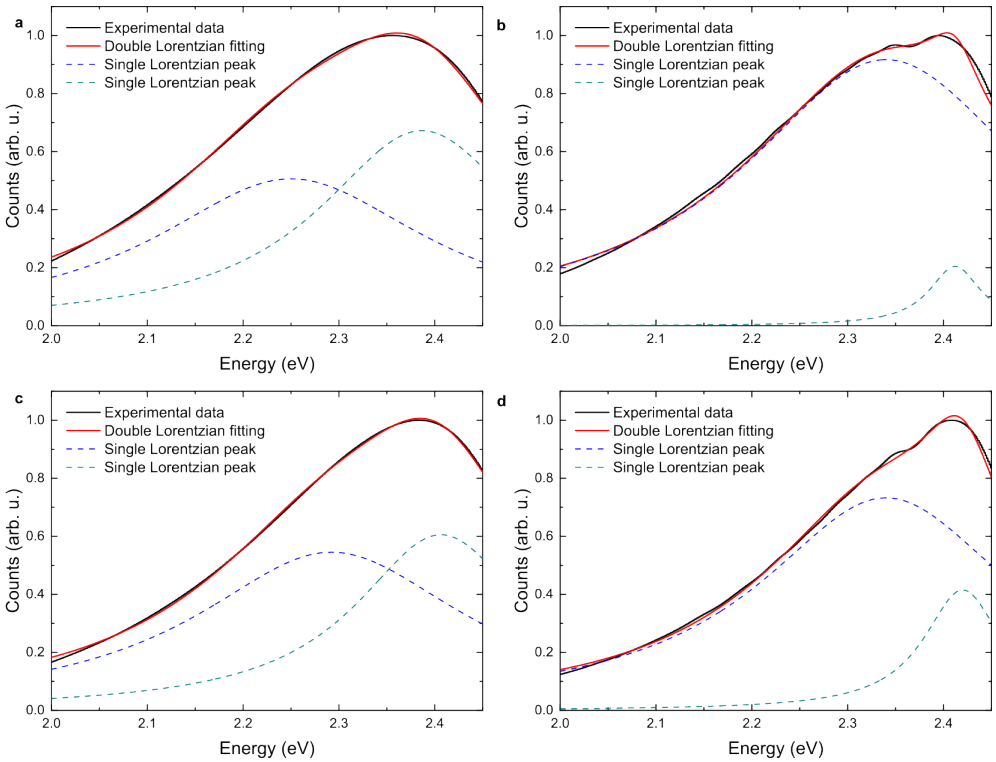

Fig. S4 Simulated scattering spectra of Ag CNPs. Scattering spectra for Ag CNPs with edge lengths of 85 nm (**a**,**b**) and 80 nm (**c**,**d**). Panels **a** and **c** show simulations at room temperature, whereas **b** and **d** present the corresponding spectra at 10 K.

Theoretical model

We model a two-level emitter (exciton) coupled to a single plasmonic mode. We work in the cavity rotating frame and set $\hbar = 1$. The detuning is

$$\Delta = \omega_c - \omega_x,$$

with ω_c and ω_x given by the cavity and exciton frequency, respectively. The Jaynes–Cummings (JC) Hamiltonian reads

$$H \;=\; -\Delta\,\sigma^\dagger\sigma \;+\; g\,(a^\dagger\sigma + a\,\sigma^\dagger), \tag{S2}$$

where a ($a^\dagger$) is the cavity annihilation (creation) operator, and σ ($\sigma^\dagger$) is the exciton lowering (raising) operator [2]. An open-system dynamics follows the Lindblad master equation

$$\dot\rho \;=\; -i[H,\rho] \;+\; \sum_j \mathscr{D}[C_j]\rho, \qquad \mathscr{D}[C]\rho \equiv C\rho C^\dagger - \tfrac{1}{2}\{C^\dagger C,\rho\}. \tag{S3}$$

While collapse channels are as follows:

$$C_\kappa = \sqrt{\kappa}\,a \qquad \text{(cavity energy decay)}, \tag{S4}$$

$$C_\gamma = \sqrt{\gamma}\,\sigma \qquad \text{(exciton radiative decay)}, \tag{S5}$$

$$C_\phi = \sqrt{\gamma_\phi/4}\,\sigma_z \qquad \text{(pure dephasing)}, \tag{S6}$$

$$C_{P_c} = \sqrt{P_c}\,a^\dagger, \quad C_{P_x} = \sqrt{P_x}\,\sigma^\dagger \qquad \text{(incoherent pumps)}. \tag{S7}$$

With this convention, the exciton homogeneous linewidth is

$$W_x \simeq \gamma + \gamma_\phi,$$

and the optical coherence time is $T_2 \simeq 2/W_x$.

Steady-state spectra are computed from two-time correlation functions using the quantum regression theorem employing Python QuTiP v5.2.1 [3]. In the cavity frame,

$$S_{\rm cav}(\omega;\Delta) = \frac{F_{\rm cav}\kappa}{2\pi}\;\mathrm{Re}\int_0^\infty dt\,e^{i\omega t}\,\langle a^\dagger(t)\,a(0)\rangle_{\rm ss}, \tag{S8}$$

$$S_{\rm rad}(\omega;\Delta) = \frac{F_{\rm rad}\gamma}{2\pi}\;\mathrm{Re}\int_0^\infty dt\,e^{i\omega t}\,\langle \sigma^\dagger(t)\,\sigma(0)\rangle_{\rm ss}. \tag{S9}$$

Here $F_{\rm cav}$ and $F_{\rm rad}$ are geometry/collection weights. For detection without a fixed interferometric phase, the measured spectrum is well described by the incoherent sum

$$S_{\rm det}(\omega;\Delta) \;=\; S_{\rm cav}(\omega;\Delta) + S_{\rm rad}(\omega;\Delta). \tag{S10}$$

In the absence of pumping, the complex normal-mode frequencies are eigenvalues of the effective non-Hermitian matrix:

$$\begin{pmatrix} \omega_c - i\kappa/2 & g \\ g & \omega_x - i\Gamma/2 \end{pmatrix}, \qquad \Gamma \equiv \gamma + \gamma_\phi.$$

At $\Delta = 0$ the observable splitting is given by:

$$\Delta\omega_{\text{obs}} \;=\; 2\,\text{Re}\left[\sqrt{g^2 - \tfrac{(\kappa-\Gamma)^2}{16}}\right], \tag{S11}$$

withe the criteria $g > (\kappa + \Gamma)/4$ (for resolvable splitting) and $2g > |\kappa - \Gamma|$ (for underdamped temporal oscillations) following directly the literature [4–6].
For $\Delta \neq 0$ equation S11 transforms into the following form:

$$g \;=\; \frac{1}{2}\sqrt{\Delta\omega_{\text{obs}}^2 - \Delta^2 + \frac{(\kappa-\Gamma)^2}{4}}, \tag{S12}$$

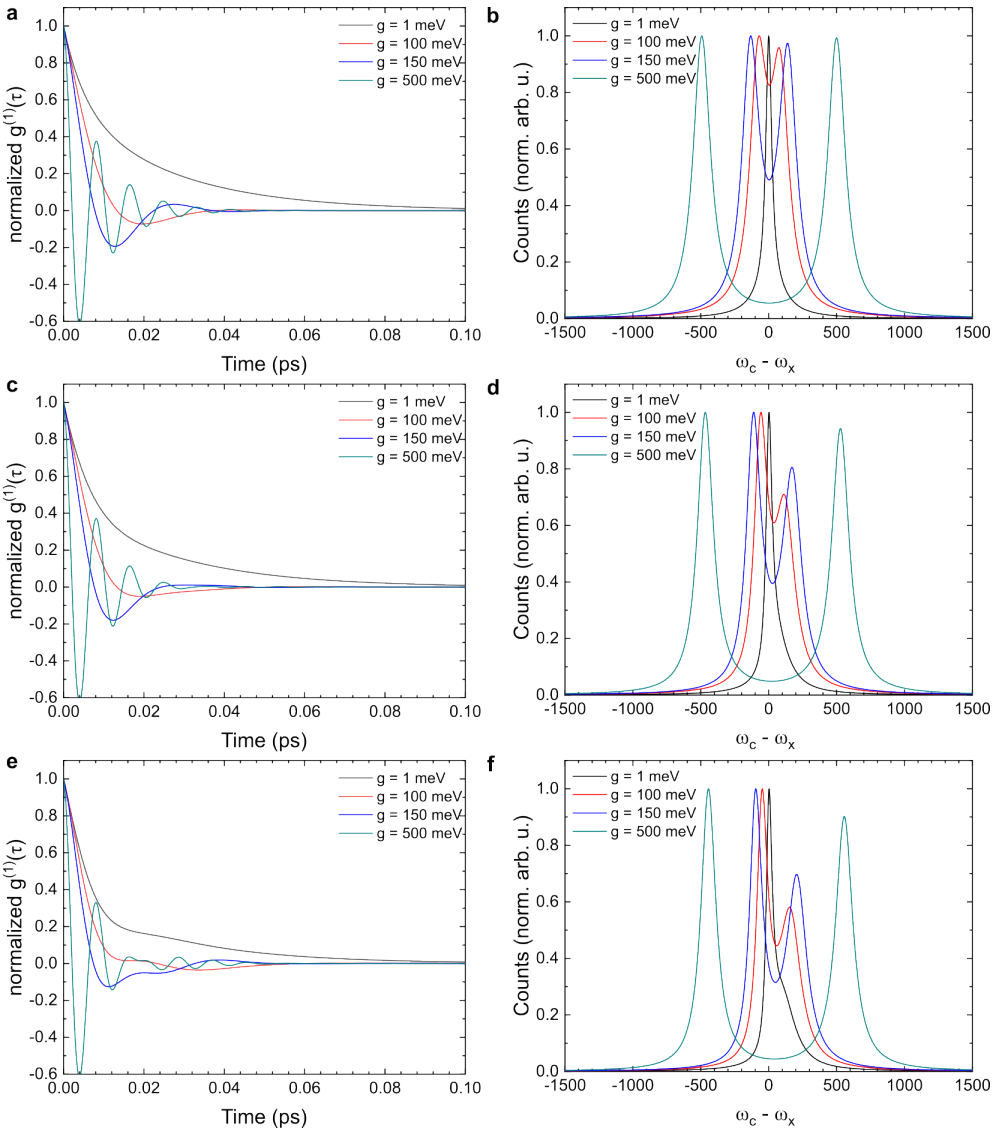

Fig. S5 Simulated time- and frequency-domain response of the coupled exciton–plasmon systems. a,c,e, Temporal evolution of the cavity population $\langle a^\dagger a \rangle(t)$ computed within the Jaynes–Cummings model for increasing coupling strengths (g = 1, 100, 150, and 500 meV). **b,d,f,** Corresponding Fourier-transformed S_{det} spectra revealing the emergence of Rabi splitting as g increases. Panels (**a,b**), (**c,d**), and (**e,f**) correspond to Ag CNPs with diameters a = 85, 80, and 75 nm, respectively.

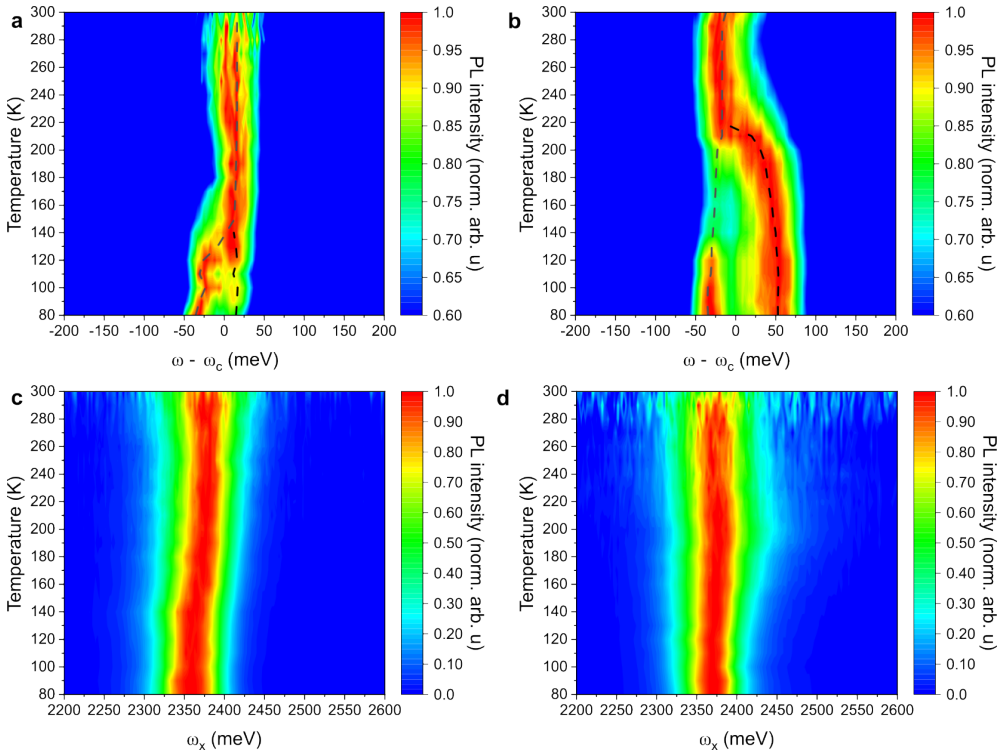

Fig. S6 Normalized temperature-dependent PL spectra. a–d, PL spectral maps of $CsPbBr_3$/Ag composites with CNP side lengths of 85 nm (**a**), 80 nm (**b**), and 75 nm (**c**), along with a reference sample (**d**), measured over a temperature range of 80–300 K. Black dashed lines serve as guides to the polariton positions. Spectra were shifted along the energy axis such that the zero-detuning polariton splitting aligns at 0 meV.

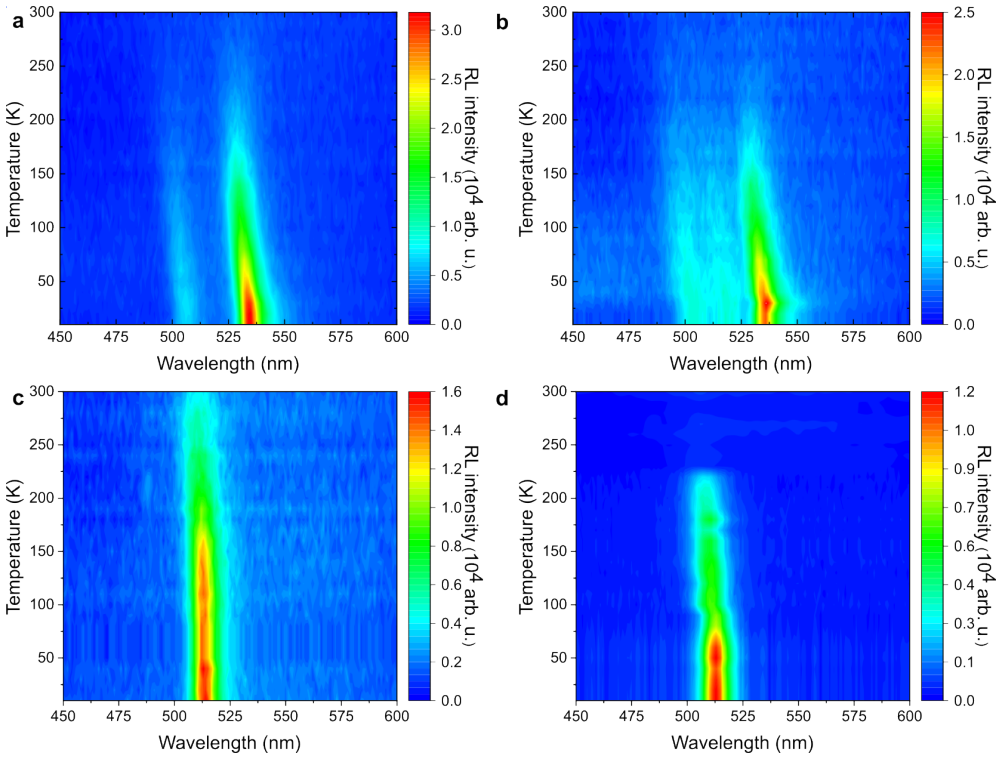

Fig. S7 Raw temperature-dependent radioluminescence (RL) spectra of $CsPbBr_3$/Ag composites. Maps are shown for composites with CNP side lengths of **a**, 85 nm; **b**, 80 nm; **c**, 75 nm; and for a reference sample, **d**. All measurements were performed over a temperature range of 10–300 K.

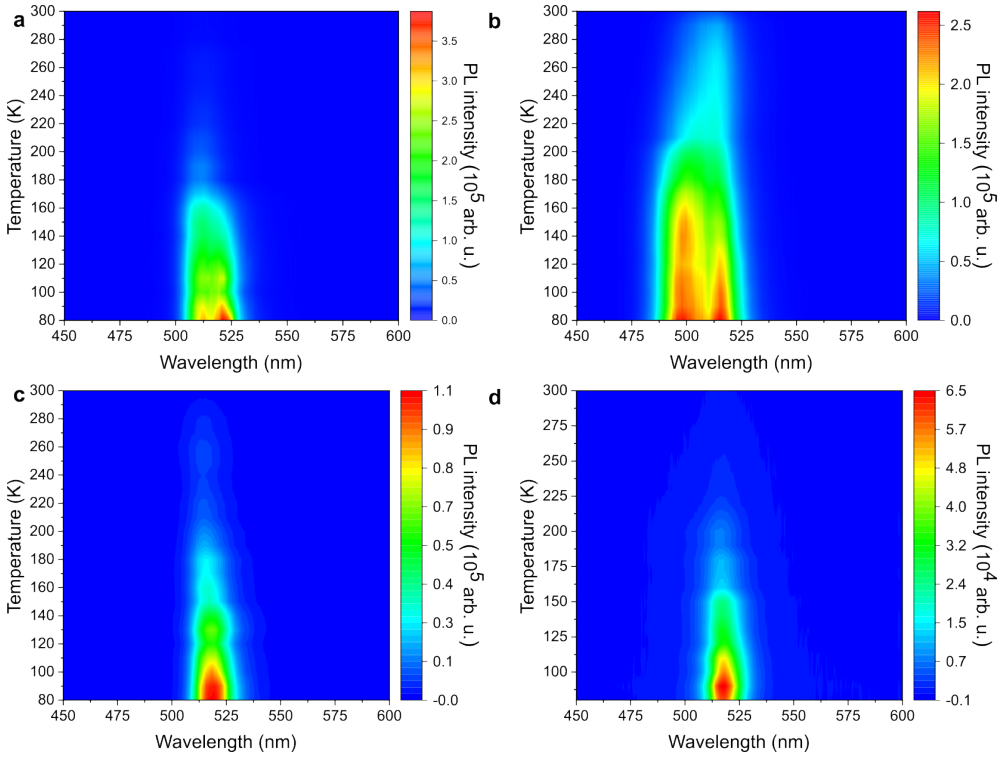

Fig. S8 Raw temperature-dependent PL spectra of $CsPbBr_3$/Ag composites. a–d, Maps for CNP side lengths of 85 nm (**a**), 80 nm (**b**), and 75 nm (**c**), and a reference sample (**d**), measured from 80–300 K.

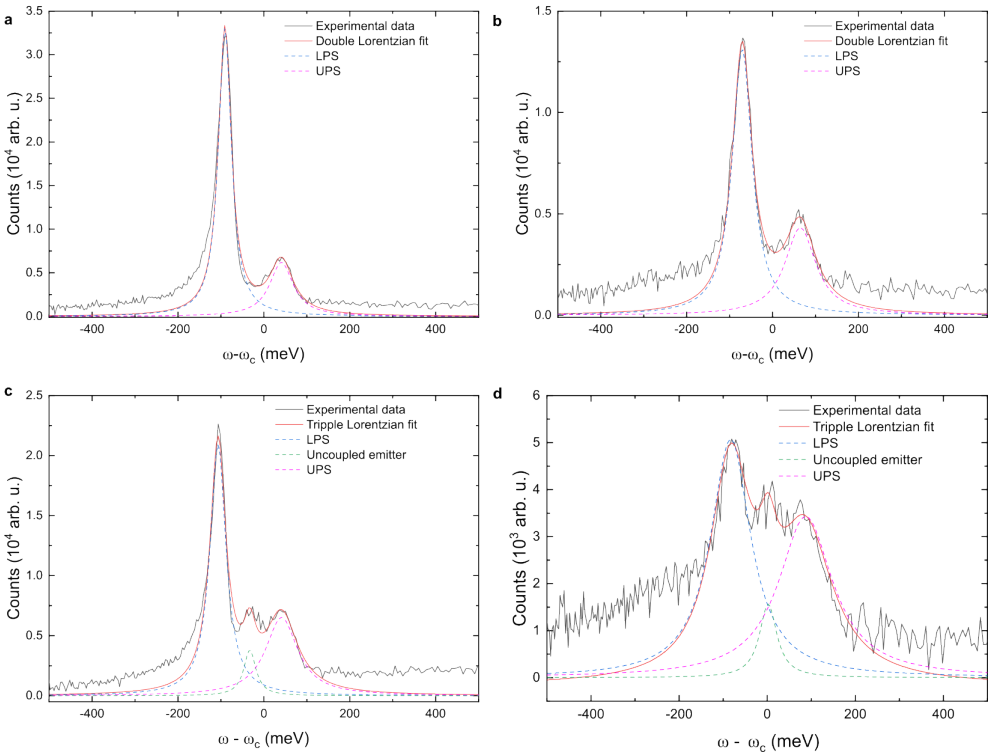

Fig. S9 The fits of RL spectra of $CsPbBr_3$/Ag composites at low temperature and zero detuning. RL spectra of $CsPbBr_3$/Ag composites with CNP side length of 85 nm measured at 10 K (**a**) and at the effective zero-detuning temperature of 100 K (**b**). RL spectra of $CsPbBr_3$/Ag composites with CNP side length of 80 nm measured at 10 K (**c**) and at the effective zero-detuning temperature of 130 K (**d**). All spectra include Lorentzian-function fits.

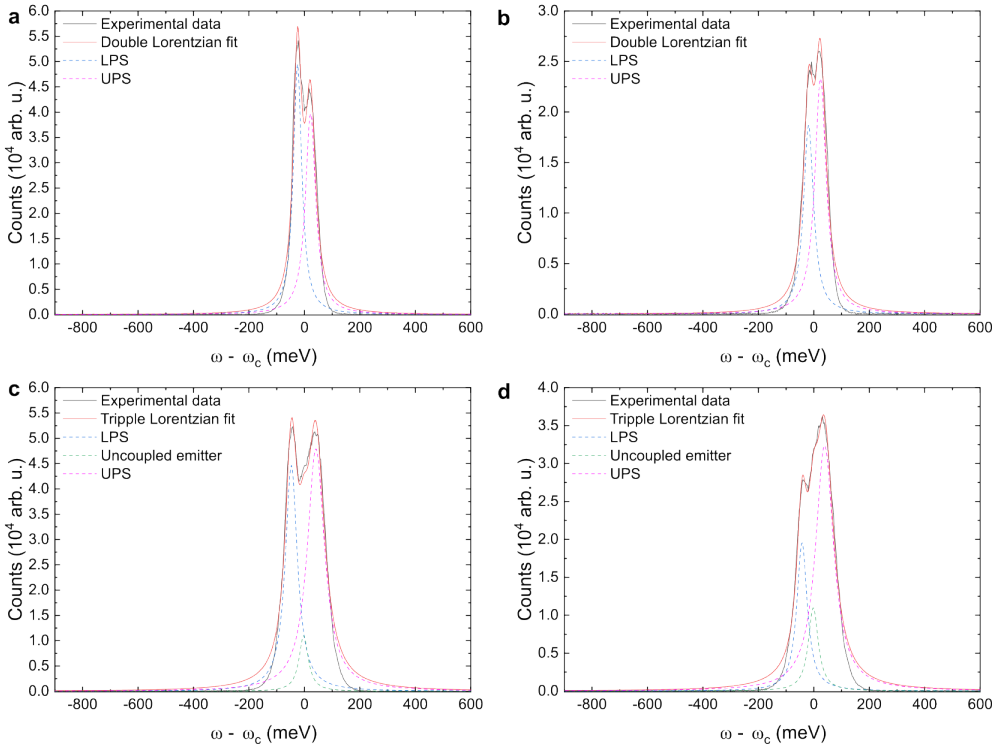

Fig. S10 The fits of PL spectra of $CsPbBr_3$/Ag composites at low temperature and zero detuning. PL spectra of $CsPbBr_3$/Ag composites with a CNP side length of 85 nm measured at (**a**) 80 K and at the effective zero-detuning temperature (**b**) 100 K. Corresponding spectra for composites with a CNP side length of 80 nm measured at (**c**) 80 K and (**d**) 130 K. All spectra include Lorentzian function fits.

Table S1 Extracted coupling parameters for $CsPbBr_3$/Ag CNPs composites. The grey-shaded columns emphasise the most relevant indicators of the coupling regime, namely g, and SC^+.

	$\Delta\omega_{obs}$ (meV)	Δ (meV)	κ (meV)	γ (meV)	g (meV)	SC^+ (meV)	C	g/ω_x
CNP side length = 85 nm								
PL	55	8.6	345	61	76	101	1.09	0.032
RL	147	-6	259	52	89	77	2.39	0.036
CNP side length = 80 nm								
PL	95	46	325	61	78	96.5	1.22	0.032
RL	168	-61	244	52	98	74	2.65	0.037

Uncertainties of each parameter are lower than 10% of the value and are not included in the table for better clarity.

The experimental time-resolved photoluminescence (TRPL) decays were fitted using a sum of three exponential components according to

$$I(t) = \sum_{i=1}^{3} A_i \exp\left(-\frac{t}{\tau_i}\right), \tag{S13}$$

where A_i are the amplitudes of the individual decay components, and τ_i denote their characteristic lifetimes.

The fractional contribution of each component to the total emission is defined as

$$f_i = \frac{A_i \tau_i}{\sum_{j=1}^{3} A_j \tau_j}, \tag{S14}$$

while the intensity-weighted average lifetime is given by

$$\langle \tau \rangle = \frac{\sum_{i=1}^{3} A_i \tau_i^2}{\sum_{i=1}^{3} A_i \tau_i}. \tag{S15}$$

All parameters (A_i, τ_i) were treated as free variables and optimised by nonlinear least-squares fitting using the `curve_fit` routine from the SciPy library [1].

Exciton-plasmon coupling rate

The exciton-plasmon coupling strength g between the $CsPbBr_3$ NPLs excitons and the LSPR of the Ag CNPs was evaluated using the standard dipole-field interaction formalism [7]. For a collection of N coherently interacting excitonic oscillators coupled to a single plasmonic mode, the coupling rate is given by

$$g = \mu \sqrt{\frac{4\pi\hbar N c}{\lambda\, \varepsilon\, \varepsilon_0\, V_{\text{eff}}}}. \tag{S16}$$

In this expression, μ denotes the transition dipole moment of a single exciton, while N represents the number of excitons within the plasmonic near-field region participating in the coherent interaction. The parameter λ corresponds to the exciton

resonance wavelength, taken here as the peak emission wavelength of the $CsPbBr_3$ nanoplatelets. The dielectric response of the surrounding medium is described by the product $\varepsilon\varepsilon_0$, where ε is the static relative permittivity of the polymer matrix embedding the nanocubes and ε_0 is the vacuum permittivity. The quantity V_{eff} denotes the effective mode volume of the plasmonic cavity extracted from finite-difference time-domain (FDTD) simulations, and c and $\hbar$ are the speed of light and the reduced Planck constant, respectively. Equation S16 reflects the collective nature of the coupling through its $\sqrt{N}$ scaling and the enhancement of the local electric field through its $1/\sqrt{V_{\text{eff}}}$ dependence.

For quantitative estimates of g, we adopt physically justified parameter values. The exciton transition dipole moment is taken to be consistent with the experimentally measured range of $\mu \approx$ 10-13 D reported for strongly confined two-dimensional lead-halide perovskites using high-precision optical Stark spectroscopy[8]. Although the referenced studies concern layered perovskite quantum wells rather than colloidal $CsPbBr_3$ nanoplatelets, the degree of quantum confinement and the predominantly in-plane dipole orientation are closely analogous.

To determine the number of excitons participating in the coherent interaction, we use the areal exciton density σ_{exc} appropriate for low-excitation, linear-response conditions. For the $CsPbBr_3$ nanoplatelets studied here, we adopt σ_{exc} from $= 10^{11}$ cm^{-2} to $= 10^{12}$ cm^{-2}, for weak optical or ionising-radiation excitation, respectively[9]. This density corresponds to the probability of generating at most one exciton per nanoplatelet, consistent with the absence of nonlinear signatures in the PL and RL spectra. The total number of contributing excitons is then obtained as

$$N = \sigma_{\text{exc}}\, A_{\text{eff}},$$

where A_{eff} is the simulated effective interaction area of the plasmonic near field associated with a given nanocube size.

The dielectric constant was taken as $\varepsilon = 3.6$ to reflect the optical permittivity of the PDMS matrix in contact with the nanocubes. The exciton resonance wavelength was set to $\lambda = 518$ nm according to the room-temperature PL peak of the nanoplatelets. The effective mode volumes V_{eff} were obtained from FDTD simulations for each nanocube edge length.

Table S2 Parameters for coupling strength calculations in Eq. S16. Effective interaction area A_{eff} and mode volumes V_{eff} for Ag CNPs extracted from FDTD simulations for different edge lengths a.

a (nm)	A_{eff} (μm^2)	V_{eff} (μm^3)
75	2.2×10^{-3}	3.92×10^{-7}
80	2.3×10^{-3}	4.13×10^{-7}
85	2.4×10^{-3}	4.37×10^{-7}
90	2.5×10^{-3}	4.64×10^{-7}

References

[1] Virtanen, P., Gommers, R., Oliphant, T.E., Haberland, M., Reddy, T., Cournapeau, D., Burovski, E., Peterson, P., Weckesser, W., Bright, J., van der Walt, S.J., Brett, M., Wilson, J., Millman, K.J., Mayorov, N., Nelson, A.R.J., Jones, E., Kern, R., Larson, E., Carey, C.J., Polat, İ., Feng, Y., Moore, E.W., VanderPlas, J., Laxalde, D., Perktold, J., Cimrman, R., Henriksen, I., Quintero, E.A., Harris, C.R., Archibald, A.M., Ribeiro, A.H., Pedregosa, F., van Mulbregt, P., SciPy 1.0 Contributors: SciPy 1.0: Fundamental algorithms for scientific computing in python. Nat. Methods **17**(3), 261–272 (2020) https://doi.org/10.1038/s41592-019-0686-2

[2] Jaynes, E.T., Cummings, F.W.: Comparison of quantum and semiclassical radiation theories with application to the beam maser. Proc. IEEE **51**(1), 89–109 (1963) https://doi.org/10.1109/PROC.1963.1664

[3] Lambert, N., Giguère, E., Menczel, P., Li, B., Hopf, P., Suárez, G., Gadhvi, R., Agarwal, R., Galicia, A., Shammah, N., Nation, P., Johansson, J.R., Ahmed, S., Cross, S., Pitchford, A., Nori, F.: Qutip 5: The quantum toolbox in python (2024) https://doi.org/arXiv:2412.04705

[4] Houdré, R., Stanley, R.P., Ilegems, M.: Vacuum-field rabi splitting in the presence of inhomogeneous broadening. Phys. Rev. A **53**, 2711–2715 (1996) https://doi.org/10.1103/PhysRevA.53.2711

[5] Törmä, P., Barnes, W.L.: Strong coupling between surface plasmon polaritons and emitters: a review. Rep. Prog. Phys. **78**(1), 013901 (2015) https://doi.org/10.1088/0034-4885/78/1/013901

[6] Niu, Y., Xu, H., Wei, H.: Unified scattering and photoluminescence spectra for strong plasmon–exciton coupling. Phys. Rev. Lett. **128**, 167402 (2022) https://doi.org/10.1103/PhysRevLett.128.167402

[7] Yu, J., Hou, S., Sharma, M., Tobing, L.Y.M., Song, Z., Delikanli, S., Hettiarachchi, C., Zhang, D., Fan, W., Birowosuto, M.D., Wang, H., Demir, H.V., Dang, C.: Strong plasmon–wannier mott exciton interaction with high aspect ratio colloidal quantum wells. Matter **2**, 1550–1563 (2020) https://doi.org/10.1016/j.matt.2020.03.013

[8] Proppe, A.H., Yang, F., Choi, H., Voznyy, O., Walters, G., Quintero-Bermudez, R., Tan, H., Kelley, S.O., Sargent, E.H.: Picosecond photogenerated carrier recombination dynamics in metal halide perovskite quantum wells probed by the optical stark effect. J. Phys. Chem. Lett. **11**(7), 3331–3337 (2020) https://doi.org/10.1021/acs.jpclett.0c00845

[9] Shcherbakov-Wu, W., Saris, S., Sheehan, T.J., Wong, N.N., Powers, E.R., Krieg, F., Kovalenko, M.V., Willard, A.P., Tisdale, W.A.: Persistent enhancement of exciton diffusivity in $cspbbr_3$ nanocrystal solids. Sci. Adv. **10**(8), 6320 (2024)

https://doi.org/10.1126/sciadv.adj6320